Vibrational properties of 2H-PbI_2 semiconductors studied via Density Functional Theory calculations

Laurent Pedesseau, Jacky Even, Claudine Katan, Faical Raouafi, Y. Wei, Emmanuelle Deleporte, Jean-Marc Jancu

To cite this version:

Laurent Pedesseau, Jacky Even, Claudine Katan, Faical Raouafi, Y. Wei, et al.. Vibrational properties of 2H-PbI_2 semiconductors studied via Density Functional Theory calculations. Thin Solid Films, 2013, Current Trends in Optical and X-Ray Metrology of Advanced Materials for Nanoscale Devices III, 541, pp.9-11. 10.1016/j.tsf.2012.10.129 . hal-01864417

HAL Id: hal-01864417
https://hal.science/hal-01864417v1

Submitted on 3 Jul 2024

extended version of Thin Solid Films 541 (2013) 9–11; https://doi.org/10.1016/j.tsf.2012.10.129

Density-functional theory characterization of 2H-$\mathrm{PbI_2}$

L. Pedesseau,[1,*] F. Raouafi,[2] Y. Wei,[3] C. Katan,[1] J. Even,[1] E. Deleporte,[3] and J.-M. Jancu[1]
[1] *Université Européenne de Bretagne, INSA, FOTON, UMR 6082, 35708 Rennes, France*
[2] *Laboratoire de Physico-chimie des Matériaux Polyméres,*
Institut Préparatoire aux Études Scientifiques et Techniques, BP51, 2070 La Marsa, Tunisia
[3] *Laboratoire de Photonique Quantique et Moléculaire, École normale Supérieure de Cachan,*
61 Avenue du Président Wilson, 94235 Cachan Cedex, France

(Dated: March 30, 2012)

version 0.0.2

We perform a detailed density functional theory investigation of the lattice dynamics and excitation spectra of the 2H-$\mathrm{PbI_2}$ semiconductor. We model the Born effective charge, optical and static dielectric tensors, phonon frequencies, and Raman spectrum within the density functional perturbation theory and the local density approximation in a plane-wave pseudopotential formalism. The static tensor is found strongly anisotropic along the vertical axis of the crystal related to the polar phonon and the $\mathrm{E_u}$ mode at the Γ point. The band structure and complex dielectric functions are calculated from the G0W0 approximation and the Bethe-Salpeter equation and compare well with our spectroscopic measurements. A very substantial enhancement of the exciton effects near the band edge with respect to sp-bonded semiconductors is demonstrated. Our results are in overall agreement with experiment and consistent with other pseudopotential calculations when available.

PACS numbers: 62.20.-x, 63.20.D-, 71.15.Mb, 71.35.-y, 77.22.-d, 78.20.-e, 78.30.-j

I. INTRODUCTION

Inorganic-organic hybrid quantum structures represent new routes in solid-state chemistry and optoelectronic devices [1]. Among these systems, layered halide perovskites have attracted attention over the last few years due to the interplay between the inorganic and organic characteristics within a molecular-scale composite, which makes them into a versatile, highly usable, and attractive molecular materials for nanophotonic devices. This is due to the inorganic part forms an extended framework bound from the covalent/ionic interactions that provide high carrier mobilities whereas the organic part facilitates self-assembly to the quantum structure. The most stringent optical property is that the electron-hole interaction is strongly enhanced by the combination of quantum and dielectric confinements over the lead iodide network, allowing for the formation of stable excitons with large binding energy even at room-temperature[2, 3]. Applications include all-optical nonlinear functionalities built upon the exciton-photon coupling in microcavity architectures [2, 4], high power light emitting diodes [5], and nanoelectronics [1]. Although there is a surge of interest in the physical properties of low-dimensional lead iodide compounds, there is little information regarding the inorganic counterpart $\mathrm{PbI_2}$. It is known that $\mathrm{PbI_2}$ is a layered semiconductor involving an atomic layer of Pb sandwiched between two layers of I atoms. The atomic structure can be stacked in variety of forms [6] due to the weak forces between sheets and the most common structure is the 2H trigonal polytype [7]. Concerning the experimental side, bulk 2H-$\mathrm{PbI_2}$ has encompassed various studies ranging from Raman spectroscopy [8–10], absorption, transmittance, reflectance, and X-ray photoemission spectra [7, 11–15]. Conversely, theoretical approaches so far have been concerned with only few empirical works [16, 17] and a detailed insight from the *ab initio* approach is still lacking. In this paper, we present first-principles density functional theory (DFT) calculations [18, 19] of the structural, elastic, dynamical, and electronic properties of 2H-$\mathrm{PbI_2}$. The paper is organized into five sections. Section II gives theoretical details of the numerical computation. Section III concerns the study of the crystalline structure, elastic constants, and bulk modulus. We examine in section IV the vibrational properties and dielectric properties. In section V, we calculate the DFT-LDA band structure with the GW corrections, the total and local density of states, the complex dielectric functions including the excitonic effects from the Bethe Salpeter equations (BSE). We also report on spectroscopic ellipsometry measurements in the photon energy-range 2-9 eV. A final section concludes.

II. COMPUTATIONAL DETAILS

Total energy DFT calculations are carried out by means of the *ab initio* ABINIT code [20] within the local density approximation (LDA) [21]. A plane-wave basis set with an energy cutoff of 950 eV is used to expand the electronic wave-functions. The reciprocal space integration is performed over 12x12x8 Monkhorst-Pack grid [22, 23]. The energy is computed from the linear response method[20] and convergence is accurately reached with tolerance on the residual potential which stems from differences between the input and output potentials. The

---

[*] laurent.pedesseau@insa-rennes.fr

crystal structure is relaxed until the forces acting on each atom are smaller than 5.10^{-5} eV/Å. The pseudopotentials are constructed from the Fritz Haber Institute (FHI) [24] format using the OPIUM code [25, 26] for Pb [$6s^2 6p^2 5d^{10}$] atom and for I [$5s^2 5p^5$] atoms. We have performed electronic band-structure calculations within DFT and corrected by the GW approximation [27, 28] where G is the Green function and W is the screened interaction. The corresponding approximation for the Green function is known as the G0W0 approximation at the first iteration of the Dyson equation. This first-order correction is known to be one of the most accurate methods for modeling spectral properties and band-gaps in solids. The vibrational density of states are studied from the density functional perturbation theory (DFPT) based on the linear response. The so-called 2n+1 theorem [29] within DFPT provides a direct access to the third-order response function and has been extensively used for semiconductors in the calculation of total-energy related properties [30–32]. Finally, the absorption spectrum is calculated by solving the Bethe-Salpeter equation (BSE) with G0W0 following the Haydock recursive procedure as described in Ref. [33].

III. STRUCTURAL PROPERTIES

A. Crystal structure

The 2H structure of PbI_2 has the trigonal space group D_{3d} with a stacking sequence *ABC* along the crystallographic z-axis or c-axis where A, B, and C each represent a separate close-packed unit of Pb-I dipole. As demonstrated by Tubbs [34], this molecular configuration is characterized by a strong intralayer chemical bonding and weak interlayer Van der Waals interactions. Modeling the Van der Waals bonding is beyond of DFT-LDA which is time-independent and consequently fails to reproduce the dynamic correlations [35]. We have performed a full optimization of the structure by minimizing the total energy with respect to the lattice constants a and c and the internal parameter u characterizing the positions of Pb and I atoms in the unit cell. While a agrees rather well with experimental data as seen in table I, a larger discrepancy is found for c and u which are expected to also depend on the weak forces along the z-axis. However, discrepancies are found within 4% of experiment, consistent with the approximations we should find in our first-principles calculations. We also note the calculated ratio c/a=1.518 differ slightly from the value 1.533 of an ideal trigonal closed-packed structure.

B. Elastic constants

2H-PbI_2 has six independent stiffness coefficients (Table II), namely, C_{11}, C_{12}, C_{13}, C_{14}, C_{33}, C_{44}, defined in cartesian coordinates, assuming a vertical (*i.e.*, 3 or z) axis of symmetry. It is well known that the trigonal symmetry has a term C_{66} which is actually depending of the others terms C_{11} and C_{12} such as $C_{66}=(C_{11}-C_{12})/2$. The diagonal term C_{11} is related to the in-plane intralayer interactions whereas C_{33} and C_{44} refer respectively to the shearing of the layers and compressibility along z-axis. In order to estimate the elastic constants, we have considered two different approaches: second-order derivatives of total energy and sound velocities constants. Actuallly, the last one is particulary useful in the present calculation (section IV E) because C_{33} and C_{44} can be directly extracted along crystal c-axis and C_{11}, C_{12} and C_{14} along the [100] direction. Table II shows that the DFT-LDA stiffness coefficients of 2H-PbI_2 compare well with available experimental data. The bulk modulus B_o can be obtained from elasticity [36]

$$B_o = \frac{(2C_{11} + C_{33}) + 2(C_{12} + 2C_{13})}{9} \tag{1}$$

or from a small hydrostatic deformation ε :

$$\Delta P = -3\varepsilon B_o \tag{2}$$

Where ε is here defined in the range of [-0.02;0.02]. We found $B_o \cong 17.3$GPa to be compared to the experimental value of 15.56 GPa of Sander et al. It is known that the result of a given functional for the bulk modulus is strongly related to the behavior of lattice constants. The shorter lattice parameters give rise to higher bulk modulus as observed in our calculations.

IV. VIBRATIONAL PROPERTIES

A. Zone center

The vibrational activity of crystals is defined from the symmetry properties and atomic positions of each element. 2H-PbI_2 possesses nine vibrational modes that can be decomposed into the irreducible representations of D_{3d} space group at k=0 as follow:

$$M = A_{1g} + 2A_{2u} + 2E_u + E_g \tag{3}$$

The total mechanical representations M (3) are specific to the Wyckoff positions **1a** and **2d** of the Pb and I atom respectively. They split into 3 acoustic modes (A_{2u}+E_u) and 6 optical modes (A_{1g}+A_{2u}+E_g+E_u) decomposed as infrared active (A_{2u}+E_u) and as Raman active (A_{1g}+E_g). We point out the Raman active modes do not involve the Pb atom. The optical frequencies are illustrated in Fig. 1 with specific symmetries on a single octahedron. Two surfaces namely top and down are formed by all octahedra characterizing a crystal layer with 3 Iodine atoms localized at the vertices of equilateral triangle (figure 1). Consequently, the modes **4** and **5** belong to the same symmetry E_u and I atoms vibrate in opposition of phase of Pb. More generally, the vibration of iodine planes are found in opposition to the lead plane. The modes **6** (E_g), **7**(E_g), and **8**(A_{1g}), are specific to the Raman mode corresponding to a static lead atom vibrating in opposite phase of iodine planes. Finally, the mode **9**(A_{2u}) results from the combination of an orthogonal vibration of iodine surfaces to the lead plane.

B. Optical dielectric tensor and Born Charge tensors

It is of interest to apply local-density functional theory framework to study dielectric and piezoelectric properties of inorganic materials. Objective is to provide a microscopic understanding of the factors that can lead to enhanced performance. In particular, the key quantities that determine the piezoelectric constants are the atomic response to macroscopic strain and Born effective charge tensors. With respect to the trigonal symmetry, the dielectric and Born charge tensors are anisotropic with two equal components in the xy-plane: $\epsilon^\infty_\parallel$ and $Z^n_\parallel$, and a distinct value along the z-axis: $\epsilon^\infty_\perp$ and $Z^n_\perp$.

Dugan and Henisch [37] measured the dielectric constants of 2H-PbI_2 at low temperature and found a less ionic character than hitherto supposed by using transmission interference fringes [38]. More recently, infrared reflectivity measurements [39] have evidenced the nature of intralayer forces, indicating a frequency anisotropy of long-wavelength transverse optical (TO) phonons for the A_{2u} and E_u modes orthogonal to the xy-plane. The dielectric and Born charge tensors, although often difficult to measure, can be analyzed in theoretical point of view. Here, we model the dielectric tensor ϵ^∞_{ij} from the second-order derivatives of the total energy with respect to an external electric field. Technical details can be found in [40]. The resulting matrix are found to be diagonal as predicted by the symmetry analysis with: $\epsilon^\infty_\parallel$=7.85 and $\epsilon^\infty_\perp$=6.35. Our calculations also compare well the experimental results of $\epsilon^\infty_\parallel$=6.1 and $\epsilon^\infty_\perp$=5.31 at room temperature [39], and $\epsilon^\infty_\perp$=6.2 measured by Dugan in Ref. [37].

We have calculated the Born effective charge tensors [40] with respect to the acoustic sum rule. It guarantees charge neutrality on the atomic species with a direct relationship between the electric field and displacements of atoms :

$$Z^n_{ij} = \frac{\partial F^n_i}{e\partial E_j} \qquad \text{with} \begin{cases} n \equiv Pb, I \\ i, j \equiv x, y, z \\ \sum_n Z^n_{ij} = 0 \end{cases} \tag{4}$$

where F^n_i is the force acting on atom n in the i direction and E_j represents the electric field along the j direction.

Our results shown in Table III, are more anisotropic than the DFT calculations of Du *etal* [41] which are performed without a minimization of the lattice constants, considering the experimental values. It is a questionable issue because a reliable description of forces and the resulting interplay with the crystalline structure can be only achieved if the lattice energy minimization is computed.

C. Static dielectric tensor

The static dielectric permittivity tensor ϵ^0 is the response both of the electronic density and crystal lattice structure to an electric field. Within the harmonic oscillator approximation, ϵ^0 can be separated into contributions arising from purely electronic screening ϵ^∞ and IR-active phonon modes ϵ^{ion} according to:

$$\epsilon^0_\bullet = \epsilon^\infty_\bullet + \epsilon^{ion}_\bullet \qquad \text{with} \begin{cases} \epsilon^{ion}_\bullet = \sum_n \epsilon^{ion,n}_\bullet \\ \epsilon^{ion,n}_\bullet = \frac{4\pi}{\Omega}\frac{S^n_\bullet}{\omega_n^2} \\ \bullet \equiv \parallel, \perp \end{cases} \tag{5}$$

where Ω is the volume of the unit cell, ω_n is the frequency, $S^n_\bullet$ is the oscillator strength of the mode n and $\epsilon^{ion,n}$ is the contribution of each individual phonon mode n.

The mode frequencies and contributions to the dielectric tensor are displayed in Table IV. Strong difference between $\epsilon^{ion,n}{}_\parallel$ and $\epsilon^{ion,n}{}_\perp$ are observed and this can be related to the values of oscillator strength and frequency of the E_u(TO) and A_{2u} modes. Actually, $\epsilon^0_\parallel$ and $\epsilon^0_\perp$ can be decomposed into 33.2% and 84.2%) of ϵ^∞ and 66.8% and 15.8% of ϵ^{ion} respectively, ensuring anisotropy in ϵ^0 with the E_u(TO) mode. This result evidences a strong electron-phonon coupling occuring in layered halide perovskites.

D. Raman spectra

2H-PbI_2 was studied by Raman techniques [8–10] but to the best of our knowledge no calculations were performed either in DFT or in an empirical context. We here purpose to clarify the attribution of each mode in connexion with the frequency and motions.

The Raman susceptibility α^v tensor is studied following the definition of Cardona [42] where the vibrational eigenmode **v** is defined as:

$$\alpha^v_{ij} = \sqrt{\Omega}\sum_n\sum_l \left.\frac{\partial\chi_{ij}}{\partial r_l}\right|_n \frac{\xi^v_{nl}}{\sqrt{m_n}}, \qquad \begin{cases} n \equiv Pb, I \\ i, j, l \equiv x, y, z \end{cases} \tag{6}$$

Ω is the volume of the primitive cell, χ_{ij} is the dielectric susceptibility tensor, r_l is the displacement of atoms n along the Cartesian axes m_n the mass of n, and ξ^v_{nl} the normalized eigenmode in the vibrational mode **v**.

In practice, Raman susceptibilities are related to the mixed third derivative of the total energy with respect to uniform electric field twice and an atomic displacement. In order to calculate them, we have performed for any direction, displacements of about ±1%. A special attention on the numerical convergence was paid in our simulations, which was reached with a 24x24x16 Monkhorst-Pack grid of k-points. Three total-energy derivatives related to the Pb atom are found equal to zero. Only those related to a single iodine (iodine 1) has to be known, also defining the second one (iodine 2). Then, the formula can be writing as:

$$\left.\frac{\partial \chi_{\mathrm{ij}}}{\partial \mathrm{r}_{\mathrm{l}}}\right|_{\mathrm{Iodine1}} = -\left.\frac{\partial \chi_{\mathrm{ij}}}{\partial \mathrm{r}_{\mathrm{l}}}\right|_{\mathrm{Iodine2}}, \quad \mathrm{i,j,l} \equiv \mathrm{x,y,z} \qquad (7)$$

Our results are given in Table V. Raman susceptibilities represent the signature of a determined vibrational mode with a specific symmetry [43]. For the iodine 1, symmetry of the $\mathrm{E_g}$ and $\mathrm{A_{1g}}$ modes are Raman allowed and the displacement pattern is within the xy-plane and along the z-axis respectively. $\mathrm{E_g}$ possesses only two different components of magnitude: 0.021 and 4.379 in unit of $(4\pi)^{-1}10^{-2}\mathrm{bohr}^{-1}$. Identically, for the $\mathrm{A_{1g}}$ mode: 5.164 and 21.208 $(4\pi)^{-1}10^{-2}\mathrm{bohr}^{-1}$. Consequently, the scattered light polarization is strongly affected by the crystal orientation where the parallel and orthogonal polarizations are defined as the horizontal-horizontal and horizontal-vertical components of the Raman spectrum respectively. Our DFT calculations are plotted in Fig. 2 with experimental data [8–10]. Magnitudes and trends are in reasonable accord with experiment except the shoulder beyond $100\mathrm{cm}^{-1}$ which is probably due to a non conventional atomic arrangement of iodine atoms.

E. Phonon dispersion and Vibrational Density of States (VDOS)

Fig. 3 shows the DFT phonon dispersion curves of 2H-$\mathrm{PbI_2}$ through the following pathway: Γ→M→L→A →Γ→K→H→. Three specific intervals are observed: [0-$46\mathrm{cm}^{-1}$], [$46\mathrm{cm}^{-1}$-$64\mathrm{cm}^{-1}$] and [$64\mathrm{cm}^{-1}$-$125\mathrm{cm}^{-1}$]. The first one is characteristic by an acoustic zone which compares well with experiment [44] for the lower frequencies (Fig. 3). For the high frequencies, agreement is qualitatively, in particular, the phonon behavior is correctly reproduced over the k-vectors. Table VI, reports on the DFT sound velocities constants together with experimental data [44]. It can be seen the theoretical results are in concordance with experiment for the longitudinal and transverse coefficients, underlying the reliability of DFT in modeling elastic constants, as already seen in section III. The second interval is identified as a frequency gap of $18\mathrm{cm}^{-1}$ at the L-point of the Brillouin zone. Finally, the optical phonon zone around $64\mathrm{cm}^{-1}$ is the most interesting part of the spectrum due to the well known (LO-TO) splitting [45, 46]. Actually, only the $\mathrm{E_u}$ and $\mathrm{A_{2u}}$ modes are involved in the current process because Pb and I atoms possess charges vibrating in opposite manner. Unfortunately, no experimental results neither simulations exist on the whole pathway except at Γ. To this end, the present optical phonon frequencies at the zone center are confronted to those of the rigid-ion model [17] and measurements [8–10, 47] in table VII. The discrepancy with experiment is of about 7.4%±5 and corresponds to the expected error inherent to the computation. splitting $\Delta\omega_{\mathrm{E_u}}^{\mathrm{LO-TO}}$ and $\Delta\omega_{\mathrm{A_{2u}}}^{\mathrm{LO-TO}}$ for the $\mathrm{E_u}$ and $\mathrm{A_{2u}}$ modes are defined as:

$$\Delta\omega_{\mathrm{S}}^{\mathrm{LO-TO}} = \sqrt{\omega_{\mathrm{S}}(\mathrm{LO})^2 - \omega_{\mathrm{S}}(\mathrm{TO})^2}, \quad \mathrm{S} \equiv \mathrm{E_u}, \mathrm{A_{2u}} \qquad (8)$$

As observed in table VII, our results closely agree with experimental data. This gives us some confidence in the prediction performed for the other k-points, but experimental tests would be of interest. We finally note the phonon anomalies are well captured in our DFT simulation in the same way of experiment [8–10, 47].

Fig. 4 shows the vibrational density of states [48] (VDOS) of 2H-$\mathrm{PbI_2}$ calculated at the Γ-point. We have modeled VDOS by using the relaxed dynamical matrix and second-order derivatives of the total-energy. The dynamical matrix possesses nine eigenvalues with six different to zero reported on table VII. The VDOS is defined by $\mathrm{g_{VDOS}}(\omega)$ as:

$$\mathrm{g_{VDOS}}(\omega) = \frac{1}{3\mathrm{N}-3}\sum_{\mathrm{v}=4}^{3\mathrm{N}} \delta(\omega - \omega_{\mathrm{v}}) \qquad (9)$$

N is the total number of atoms, **v** the vibrational mode, ω_{v} is the eigenvalue **v** of the dynamical matrix.

The resulting peaks reflect the global spectrum at the Γ-point of the whole motion which is including in Raman and infrared active modes. Three peaks are clearly identified around: $68\mathrm{cm}^{-1}$, $78\mathrm{cm}^{-1}$ and $111\mathrm{cm}^{-1}$. One can be attributed to the $\mathrm{E_u}$, $\mathrm{E_g}$, and $\mathrm{A_{2u}}$ modes respectively.

V. ELECTRONIC PROPERTIES

More detailed information on the optical properties of 2H-$\mathrm{PbI_2}$ can be obtained from the band structure and the electronic density of states (DOS). Our DFT-LDA calculations are performed at the equilibrium lattice parameters and presented in Fig. 6 for the band structure. We consider the band shape on the surface of the Brillouin zone (Fig. 5) as a crucial test of our simulations, including the wave-vector pathway connecting the surface points : Γ→ K→H→A→Γ→M→ L→A. The energy reference is set at the valence-band maximum (VBM). Since the space group of the crystal is $\mathrm{D_{3d}}$, the states with x- and y like symmetry are degenerate both at the Γ and A-points, whereas states with s-like and z-like symmetry are non degenerate. Our simulations give the VBM as A_1^+ (z-like) and the conduction-band minimum (CBM) as A_2^-

(z-like), the latter is found as A_3^- (x,y-like) in the empirical pseudopotential method (reference). Insight into the band structure may be gained through analysis of the total DOS and the local DOS (LDOS) projected on the atomic basis functions. Fig 7 reveals the energetically lowest peaks at -15 eV, -12 eV, and -7 eV are atomic-like arising from the Pb *d*, I *s*, and Pb *s* bands, respectively. The threshold at -4 eV is the absolute minimum of the fourth valence band deriving from the L-point where wave functions display sp-bonding character, in analogy to conventional semiconductors. Near the band edge, the valence maximum is mainly composed of the I *p* and Pb *s* levels whereas the Pb *p* states dominates the lowest conduction bands. A direct band gap of 1.7 eV is obtained, smaller than the measured value of 2.55 eV at low temperature [49]. This disparity is expected, since it is well known that LDA underestimates the band gaps of semiconductors. However the calculated DOS agree very well with the X-ray measurements of Scrocco et al [15], underlying the LDA description here considered is qualitatively correct. We consequently expect the LDA single-particle Hamiltonian to be a suitable reference for G0W0 to overcome LDA deficiencies, mainly for the empty states.To this end, we report on Fig. 6 the G0W0 corrections for the first valence and three first conduction states. We observe G0W0 keeps unchanged the order of symmetry of the conduction bands but corrects differently their energetic positions in the Brillouin zone. Comparing LDA and G0W0, the main effects of G0W0 are a significant increase in the fundamental gap of about 0.8eV with a slight increase in the valence bandwidth of 0.5 eV. The G0W0 gap energy is 2.65 eV, a value neglecting the spin-orbit (SO) interaction which is in concordance with experiment.

A. Dielectric function

The propose here is to give a first representation of the complex dielectric functions of 2H-PbI_2 in DFT within the many-body perturbation theory and the Bethe-Salpeter equation. The solution of BSE is obtained by using Haydocks iterative method to diagonalize the effective two-particle Hamiltonian in which the BSE is recast. We have considered 96800 transitions evolving from eleven valence and eleven conduction bands twice a mesh of 10x10x8 k-points in the Brillouin zone.

Fig. 8 shows the real ε_1 and imaginary ε_2 parts of the dielectric function for polarizations parallel and perpendicular to the optical c-axis in three cases: DFT, G0W0 and G0W0-BSE. Going on from DFT to G0W0, we observe mainly a blue-shift of the optical spectra due to G0W0 yields more accurate single-particle excitation energies and band gaps in the whole Brillouin zone. Conversely, including the excitonic effects at the BSE level, the optical gaps in the two polarizations are strongly red-shifted compared to G0W0. This a direct consequence of the low dispersion energy of the first conduction bands as evidenced in Fig. 6, giving high electron masses compared to traditional cubic semiconductor (*e.g.* GaAs). Actually, $\varepsilon_2^{\perp}$ demonstrates a huge enhancement of the first peak at approximatively 3.6eV due to the interaction electron hole pair. At the opposite, $\varepsilon_2^{\parallel}$ is clearly decreasing.

The only experiment at low temperature 77K and from electroreflectance technique was measured by Gähwiller and analysed by Kramers-Kronig dispersion. Other measures are found as [12] but the definition of polarizations was not precise. So, if we compare G0W0-BSE to experiment [11] at 77K (Fig. 9), the resonances are well described also the value of the dielectric constants. We note, however, G0W0-BSE overestimates the position of the exciton peak probably because we do not take into account the SO coupling. However, the amplitude is still well reproduced. In conclusion, even if the SO coupling is not included the position of the main experimental resonances is reproduced at the GW0-BSE level, and excitonic effects cannot be ignored in modeling the optical spectrum. Thorough analysis of Y. Nagamune *et al.* [13, 50] reported the nature of the exciton ground state of 2H-PbI_2. We have calculated the resulting characteristics at the DFT-BSE level as reported on table VIII together with the experimental findings. We found a binding energy of 34 meV different from the result $E_B^{A_1} = 63meV$ of Nagamune [13] but close to the measured value $E_B^{A_1} = 30meV$ of Le Chi Thanh [14]. Finally, the effective mass $\mu_{\perp}^{A_1}$ and exciton Bohr radius $a_o^{A_1}$ are calculated [51]. The DFT values are: 0.12m_o and 30Å, in reasonable agreement with 0.17m_o[13] and 0.08m_o[14] for the effective mass and 19Å[13] and 40Å[14] for the exciton Bohr radius.

VI. CONCLUSION

The combination of first-principles calculations and experimental measurements provide detailed information about the global properties of bulk 2H-PbI_2. The mechanical properties and elastic constants are well reproduced in the uncertainty precision of DFT.
We have employed the many body perturbation theory in the G0W0 approach to investigate the quasiparticle band structure and found a good agreement with experiment. We note however, that the spin-orbit and electron-phonon interactions, which have been neglected in this work, may play a considerable role in 2H-PbI_2. Further studies in this direction and more refined experiments are clearly needed for a more unambiguous comparison between experiment and theory.

ACKNOWLEDGMENTS

We would like to thank Matteo Giantomassi and Patrick Hermet for helpful discussions. This work was funded from the ANR project PEROCAI(ANR-10-04). The *ab initio* simulations were performed on HPC ressources of CINES and IDRIS under the allocation 2012-[x2012096724].

---

[1] C. R. Kagan, D. B. Mitzi, and C. D. Dimitrakopoulos, Science, **286**, 945 (1999).
[2] G. Lanty, A. Brehier, M. Parashkov, J. S. Lauret, and E. Deleporte, New Journal of Physics, **10**, 065007 (2008).
[3] P. A. Hobson, W. L. Barnes, D. G. Lidzey, G. A. Gehring, D. M. Whittaker, M. S. Skolnick, and S. Walker, Appl. Phys. Lett., **81**, 3519 (2002).
[4] C. Weisbuch, M. Nishioka, A. Ishikawa, and Y. Arakawa, Phys. Rev. Lett., **69**, 3314 (1992).
[5] R. B. Fletcher, D. G. Lidzey, D. D. C. Bradley, M. Bernius, and S. Walker, Appl. Phys. Lett., **77**, 1262 (2000).
[6] A. R. Verma and P. Krishna, *Polymorphism and Polytypism in Crystals* (New York: Wiley, 1966).
[7] R. S. Mitchell, Zeitschrift für Kristallographie, **117**, 309 (1962).
[8] A. Grisel and P. Schmid, physica status solidi (b), **73**, 587 (1976).
[9] W. M. Sears, M. L. Klein, and J. A. Morrison, Phys. Rev. B, **19**, 2305 (1979).
[10] B. Winkler, M. Dove, E. Salje, M. Leslie, and B. Palosz, Journal of Physics: Condensed Matter, **3**, 539 (1991).
[11] C. Gähwiller and G. Harbeke, Phys. Rev., **185**, 1141 (1969).
[12] C. Ghita, L. Ghita, I. Baltog, and M. Constantinescu, Physica Status Solidi (b), **102**, 111 (1980).
[13] Y. Nagamune, S. Takeyama, and N. Miura, Phys. Rev. B, **40**, 8099 (1989).
[14] L. C. Thanh, C. Depeursinge, F. Levy, and E. Mooser, J. Phys. Chem. Solids, **36**, 699 (1975).
[15] M. Scrocco, Journal of Electron Spectroscopy and Related Phenomena, **48**, 363 (1989).
[16] I. C. Schlüter and M. Schlüter, Phys. Rev. B, **9**, 1652 (1974).
[17] Y.-C. Chang and R. B. James, Phys. Rev. B, **55**, 8219 (1997).
[18] W. Kohn and L. J. Sham, Phys. Rev., **140**, A1133 (1965).
[19] R. Martin, *Electronic Stucture: Basic Theory and Practical Methods* (Cambridge University Press, 2004).
[20] X. Gonze, J.-M. Beuken, R. Caracas, F. Detraux, M. Fuchs, G.-M. Rignanese, L. Sindic, M. Verstraete, G. Zerah, F. Jollet, M. Torrent, A. Roy, M. Mikami, P. Ghosez, J.-Y. Raty, and D. Allan, Computational Materials Science, **25**, 478 (2002).
[21] J. P. Perdew and Y. Wang, Phys. Rev. B, **45**, 13244 (1992).
[22] H. J. Monkhorst and J. D. Pack, Phys. Rev. B, **13**, 5188 (1976).
[23] J. D. Pack and H. J. Monkhorst, Phys. Rev. B, **16**, 1748 (1977).
[24] M. Fuchs and M. Scheffler, Computer Physics Communications, **119**, 67 (1999).
[25] G. G. P. Licence, **version 3.6** ((10/2010)).
[26] I. Grinberg, N. Ramer, and A. Rappe, Phys. Rev. B, **62**, 2311 (2000).
[27] L. Hedin, Phys. Rev., **139**, A796 (1965).
[28] X. Gonze, G.-M. Rignanese, M. Verstraete, J.-M. Beuken, Y. Pouillon, R. Caracas, F. Jollet, M. Torrent, G. Zerah, M. Mikami, P. Ghosez, M. Veithen, J.-Y. Raty, V. Olevano, F. Bruneval, L. Reining, R. Godby, G. Onida, D. Hamann, and D. Allan, Zeitschrift für Kristallographie, **220**, 558 (2005).
[29] X. Gonze and J.-P. Vigneron, Phys. Rev. B, **39**, 13120 (1989).
[30] P. Giannozzi, S. de Gironcoli, P. Pavone, and S. Baroni, Phys. Rev. B, **43**, 7231 (1991).
[31] X. Gonze and C. Lee, Phys. Rev. B, **55**, 10355 (1997).
[32] S. Baroni, S. de Gironcoli, A. Dal Corso, and P. Giannozzi, Rev. Mod. Phys., **73**, 515 (2001).
[33] R. Haydock, Computer Physics Communications, **20**, 11 (1980).
[34] M. R. Tubbs, Physica Status Solidi (b), **49**, 11 (1972).
[35] V. Polo, J. Gräfenstein, E. Kraka, and D. Cremer, Chemical Physics Letters, **352**, 469 (2002).
[36] R. Hill, Proc. Phys. Soc. A, **65**, 349 (1952).
[37] A. Dugan and H. Henisch, Journal of Physics and Chemistry of Solids, **28**, 971 (1967).
[38] T. S. Moss, *Optical Properties of Semiconductors* (Butterworths, London, 1961).
[39] G. Lucovsky and R. White, Il Nuovo Cimento, **38B**, 290 (1977).
[40] P. Ghosez, J. Michenaud, and X. Gonze, Phys. Rev. B, **58**, 6224 (1998).
[41] M.-H. Du and D. J. Singh, Phys. Rev. B, **82**, 045203 (2010).
[42] M. Cardona and G. Güntherodt, *Light scattering in solids II: basic concepts and instrumentations* (Springer-Verlag Berlin and Heidelberg GmbH & Co. K, 1982).
[43] R. Loudon, Advances in Physics, **13**, 423 (1964).
[44] B. Dorner, R. E. Ghosh, and G. Harbeke, Physica Status Solidi (b), **73**, 655 (1976).
[45] H. Frölich, Proc. R. Soc. Lond. A, **160**, 230 (1937).
[46] R. H. Lyddane, R. G. Sachs, and E. Teller, Phys. Rev., **59**, 673 (1941).
[47] G. Lucovsky, R. White, W. Liang, R. Zallen, and P. Schmid, Solid State Communications, **18**, 811 (1976).
[48] D. L. Price and J. M. Carpenter, Journal of Non-Crystalline Solids, **92**, 153 (1987).
[49] M. Matuchova, K. Zdansky, J. Zavadil, A. Danilewsky, J. Maixner, and D. Alexiev, Journal of Materials Science: Materials in Electronics, **20**, 289 (2009).
[50] Y. Nagamune, S. Takeyama, and N. Miura, Phys. Rev. B, **43**, 12401 (1991).
[51] S. Chuang, *Physics of Optoelectronic Devices* (John Wiley & Sons, Inc, 1995).
[52] R. W. Wyckoff, *in Crystal Structures, 2nd edition, Vol 1* (Interscience, New York, 1963).
[53] D. Sirdeshmukh and V. Deshpande, Current Science, **41**, 210 (1972).
[54] J. Sandercock, Festkörperprobleme, **XV**, 183 (1975).

	Present DFT	Expt [52, 53]	Present Expt
a [Å]	4.46(2.2)	4.56	4.56
c [Å]	6.77(3.1)	6.98	6.99
u [/]	0.275(3.8)	0.265	0.265
c/a [/]	1.518(1.0)	1.531	1.533

TABLE I. Lattice parameters a [Å], c [Å] and the internal parameter u [/] of the $2H-PbI_2$ via DFT calculation, compared to experimental data [52, 53]. In parenthesis, errors compared to the present experimental results.

	DFT via total energy and (2n+1) theorem	DFT via sound velocities	Expt [54]	Expt [44]
C_{11} [GPa]	30.9	26.7	27.7	20.2
C_{12} [GPa]	10.5	9.7	9.6	6.1
C_{13} [GPa]	12.1	/	11.3	/
C_{14} [GPa]	4.6	/	3.0	1.8
C_{33} [GPa]	23.4	15.7	20.2	14.6
C_{44} [GPa]	8.9	5.9	6.2	5.4
B_o [GPa]	17.20	/	15.56	/

TABLE II. DFT elastic constants [GPa] and bulk modulus [GPa] of $2H-PbI_2$ compared to experimental data [44, 54].

Z^{n}_{ij}					
Present DFT work			Other theoretical studies [41]		
Pb atom (0,0,0)					
4.21	0.0	0.0	4.0	0.0	0.0
0.0	4.21	0.0	0.0	4.0	0.0
0.0	0.0	2.08	0.0	0.0	1.92
I atom ($\frac{1}{3}$,$\frac{2}{3}$,u)					
-2.105	0.0	0.0	-2.0	0.0	0.0
0.0	-2.105	0.0	0.0	-2.0	0.0
0.0	0.0	-1.04	0.0	0.0	-0.96
I atom ($\frac{2}{3}$,$\frac{1}{3}$,u)					
-2.105	0.0	0.0	-2.0	0.0	0.0
0.0	-2.105	0.0	0.0	-2.0	0.0
0.0	0.0	-1.04	0.0	0.0	-0.96

TABLE III. Present DFT Born charge tensors for each element of $2H - PbI_2$ compared to the DFT calculations of Ref. [41].

	E_u modes			A_{2u} modes		
	ω_n	$S_\parallel^n$	$\epsilon_\parallel^{\text{ion,n}}$	ω_n	$S_\perp^n$	$\epsilon_\perp^{\text{ion,n}}$
TO	64.4	8.53	12.03	111.7	2.07	0.67
LO	115.5	8.53	3.74	125.8	2.07	0.52
$\epsilon_\bullet^{\text{ion}}$		15.77			1.19	
$\epsilon_\bullet^{\infty}$		7.85			6.32	
$\epsilon_\bullet^{0}$		23.62			7.51	
$\epsilon_\bullet^{0}$ Expt[8]		26.75			6.25	
$\epsilon_\bullet^{0}$ Expt[47]		26.4			8.0	

TABLE IV. DFT frequencies ω_n in unit of $[\text{cm}^{-1}]$ of the E_u and A_{2u} modes. The oscillator strengths $S_\bullet^n$ in unit of $[10^{-5}\text{a.u.}]$ with $\bullet \equiv \parallel, \perp$ for each mode n. We report the phonon contribution $\epsilon_\bullet^{\text{ion,n}}$, the global contribution $\epsilon_\bullet^{\text{ion}}$, the electronic part $\epsilon_\bullet^{\infty}$, and the static dielectric constants $\epsilon_\bullet^{0}$, compared to measurements [8, 47].

$\left.\frac{\partial\chi_{ij}}{\partial x}\right\|_{n}$			$\left.\frac{\partial\chi_{ij}}{\partial y}\right\|_{n}$			$\left.\frac{\partial\chi_{ij}}{\partial z}\right\|_{n}$		
Pb atom (0,0,0)								
0.0	0.0	0.0	0.0	0.0	0.0	0.0	0.0	0.0
0.0	0.0	0.0	0.0	0.0	0.0	0.0	0.0	0.0
0.0	0.0	0.0	0.0	0.0	0.0	0.0	0.0	0.0
I atom ($\frac{1}{3}$,$\frac{2}{3}$,u)								
0.0	0.021	4.379	0.021	0.0	0.0	5.164	0.0	0.0
0.021	0.0	0.0	0.0	-0.021	4.379	0.0	5.164	0.0
4.379	0.0	0.0	0.0	4.379	0.0	0.0	0.0	21.208
I atom ($\frac{2}{3}$,$\frac{1}{3}$,u)								
0.0	-0.021	-4.379	-0.021	0.0	0.0	-5.164	0.0	0.0
-0.021	0.0	0.0	0.0	0.021	-4.379	0.0	-5.164	0.0
-4.379	0.0	0.0	0.0	-4.379	0.0	0.0	0.0	-21.208

TABLE V. DFPT susceptibility tensor $\left.\frac{\partial\chi_{ij}}{\partial r_l}\right|_{n}$ in unit of $[(4\pi)^{-1}\cdot 10^{-2}\cdot \mathrm{bohr}^{-1}]$ for atoms n and along the cartesian axes ($r_l \equiv (x, y, z)$) for $2H-\mathrm{PbI}_2$.

	Expt			DFT		
	V_L	V_T (in plane)	V_T (out of plane)	V_L	V_T (in plane)	V_T (out of plane)
[100]	1.86	1.07	0.94	2.02	1.12	0.97
[110]	1.81	1.10	0.86	1.72	1.15	0.67
[001]	1.54	0.93	0.93	1.55	0.95	0.95

TABLE VI. DFT sound velocities in unit of $[10^5 \mathrm{cm.s}^{-1}]$ of $2H-PbI_2$ compared to experimental data[44]

in $[\mathrm{cm}^{-1}]$	$\mathrm{E_u(TO)}$	$\mathrm{E_u(LO)}$	$\mathrm{E_g}$	$\mathrm{A_{1g}}$	$\mathrm{A_{2u}(TO)}$	$\mathrm{A_{2u}(LO)}$	$\Delta\omega^{\mathrm{LO-TO}}_{\mathrm{E_u}}$	$\Delta\omega^{\mathrm{LO-TO}}_{\mathrm{A_{2u}}}$
DFT	64.4	115.5	81.3	97.4	111.7	125.8	95.9	57.9
Rigid ion model [17]	52.6	100.1	79.4	97.8	95.4	113.2	85.2	60.9
Expt[8]	52.5	106.0	78.0	98.0	95.0	113.0	95.5	61.2
Expt[9]	52	106	78	97	96	113	91.8	59.6
Expt[10]	51.7	100.1	75.8	100.3	101.8	117.9	85.7	59.5

TABLE VII. DFT phonon frequencies of $\mathrm{2H-PbI_2}$ in cm^{-1} compared to existing theoretical studies [17] and experimental data[8–10]

	A_1[eV]	$a_o^{A_1}$[Å]	$\mu_\perp^{A_1}$[m_o]	$E_B^{A_1}$[meV]
Le Chi Thanh [14]	2.499	40	0.08	30
Y. Nagamune [13]	2.496	19	0.17	63
DFT	2.599	30±4	0.12±0.02	34±5

TABLE VIII. DFT-BSE calculations of the peak positions of the exciton levels in eV, exciton Bohr radius in Å, reduced exciton mass in m_o, and the binding energy E_B in meV.

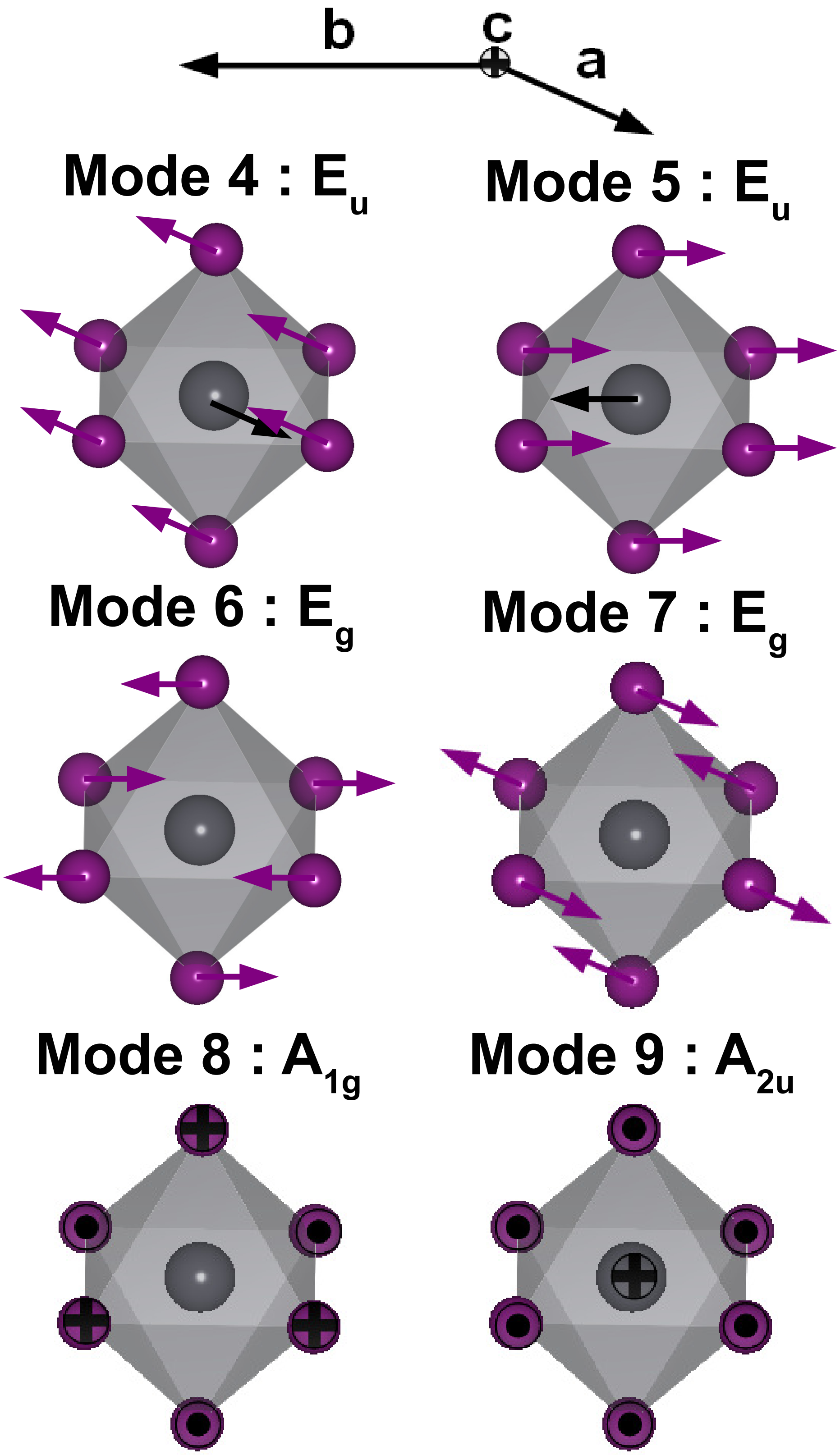

FIG. 1. Optical modes at Γ of 2H-PbI_2

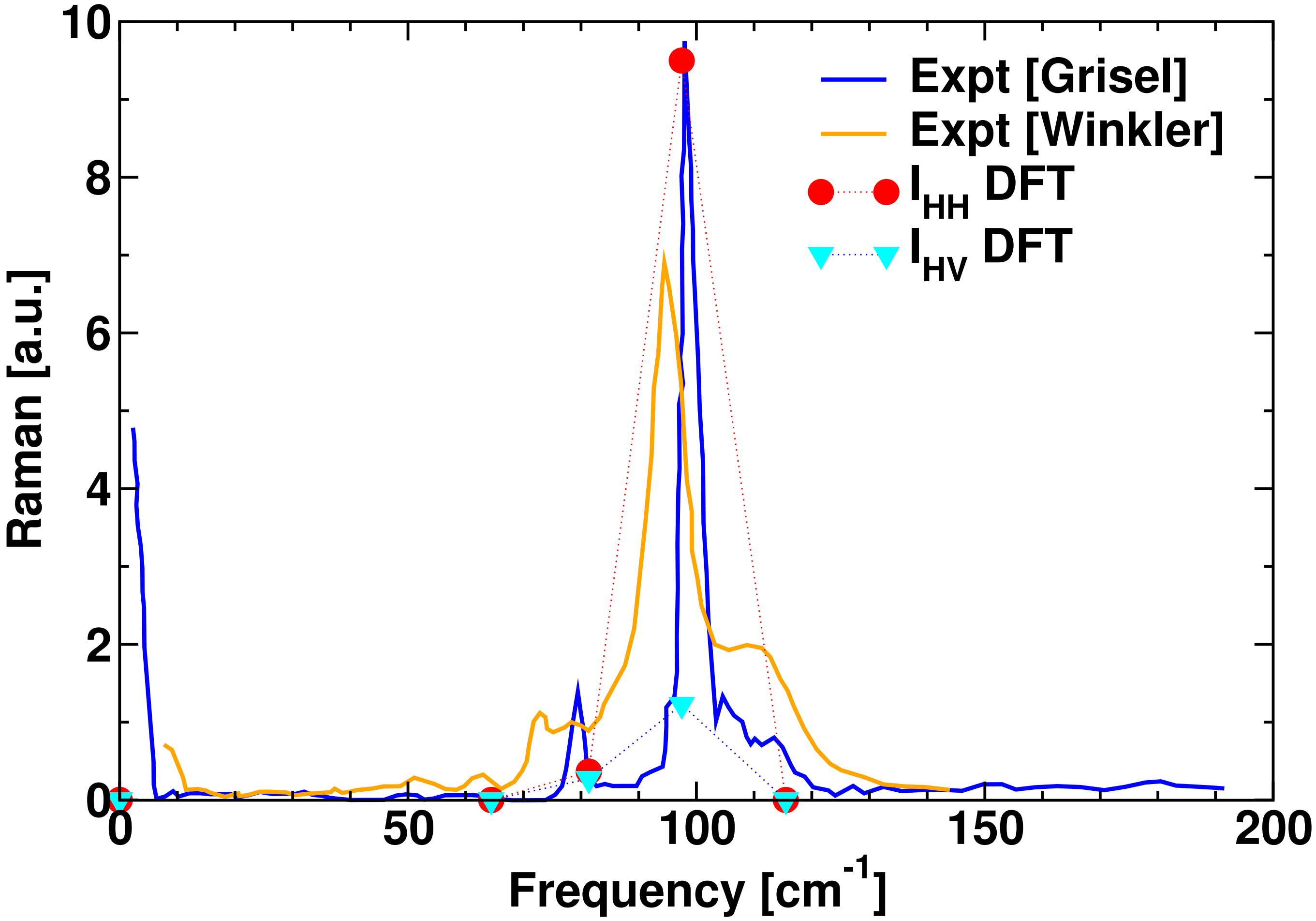

FIG. 2. Raman DFT with experiment [8–10]

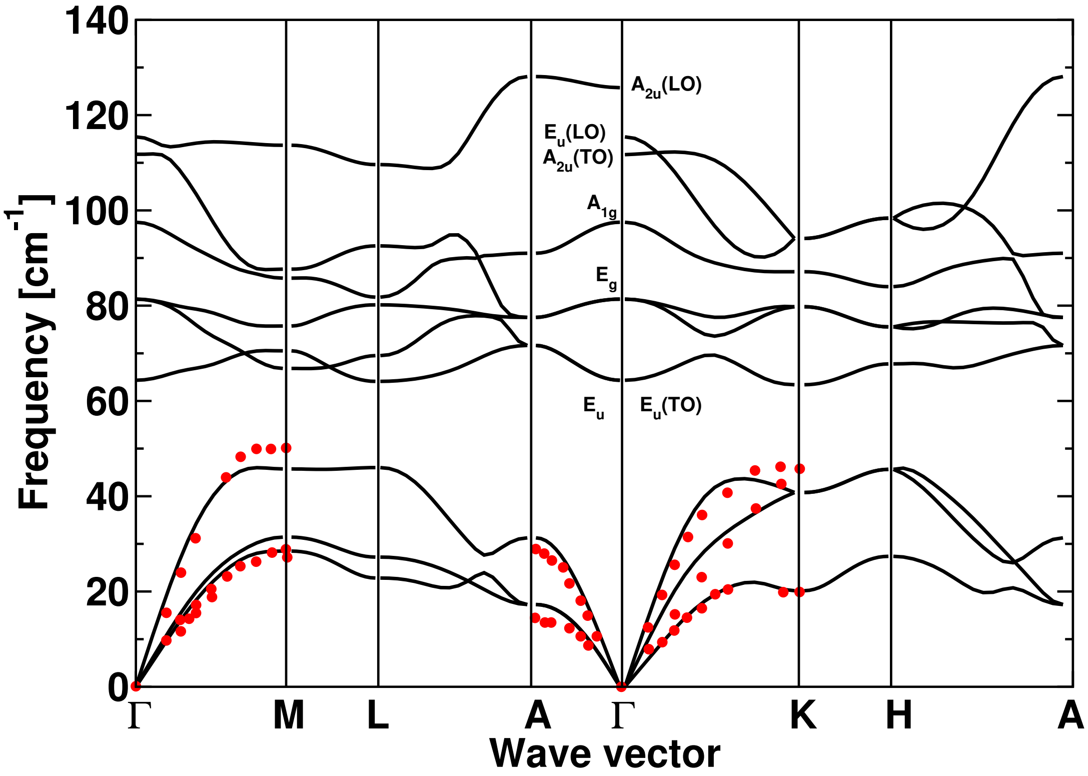

FIG. 3. Phonon of 2H-PbI$_2$ (red circles: experimental data [44]

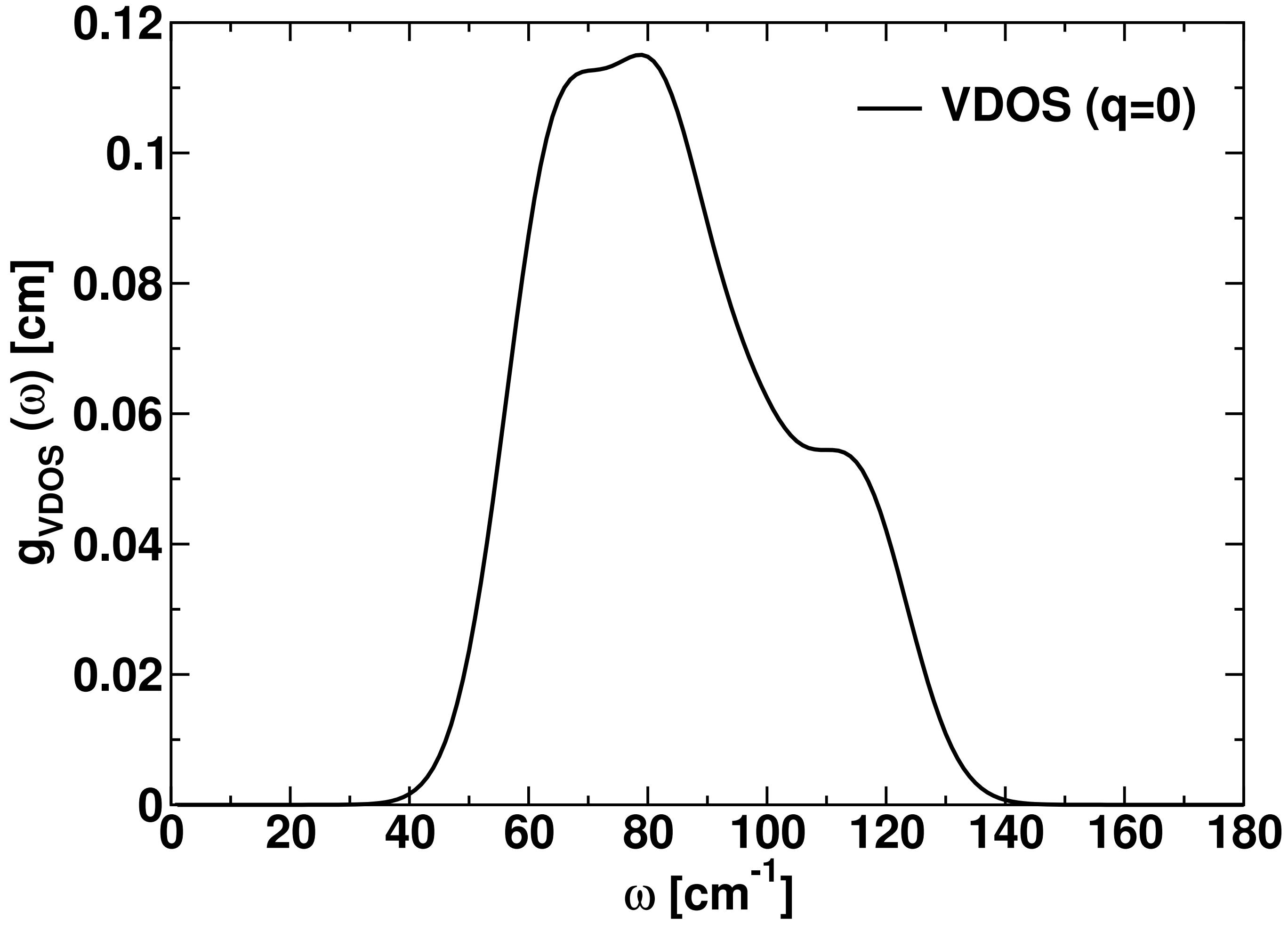

FIG. 4. Vibrational DOS at Γ of 2H-PbI$_2$

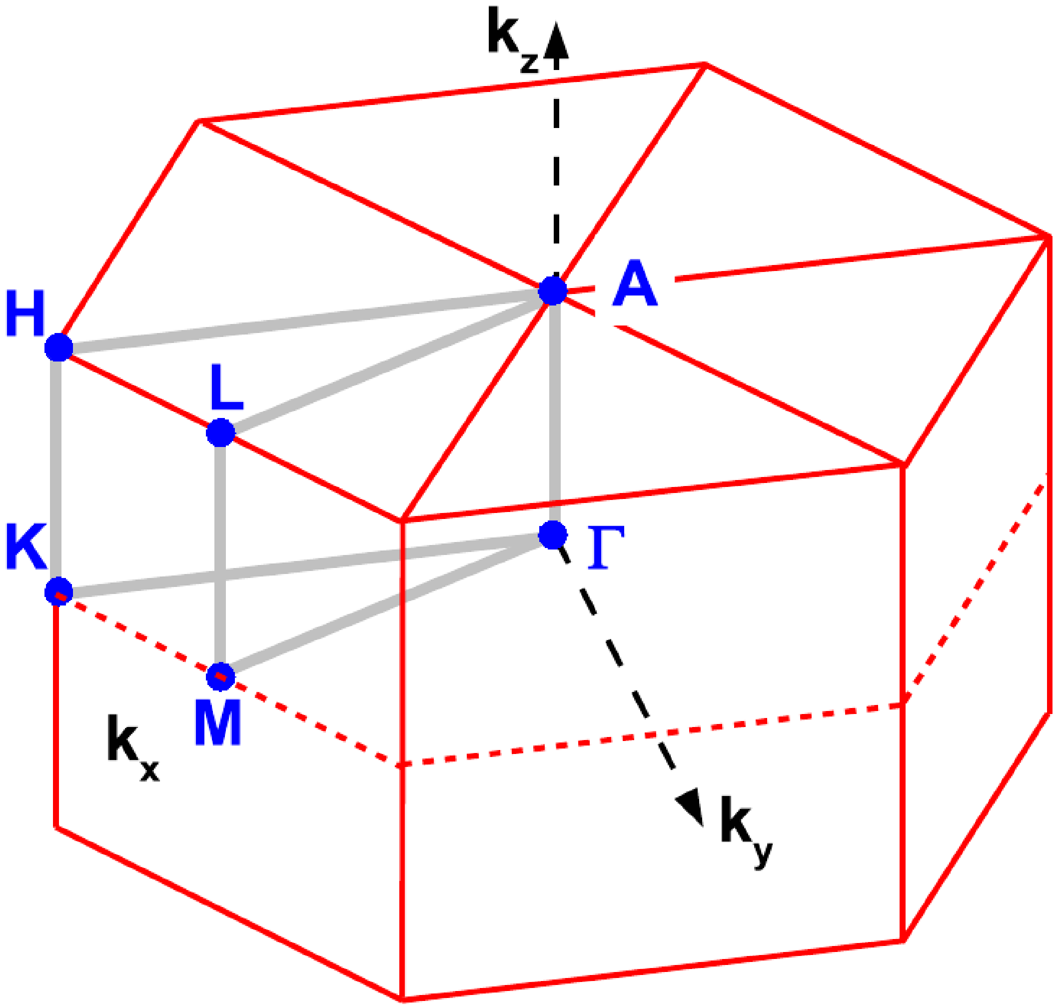

FIG. 5. Brillouin zone of 2H-PbI_2

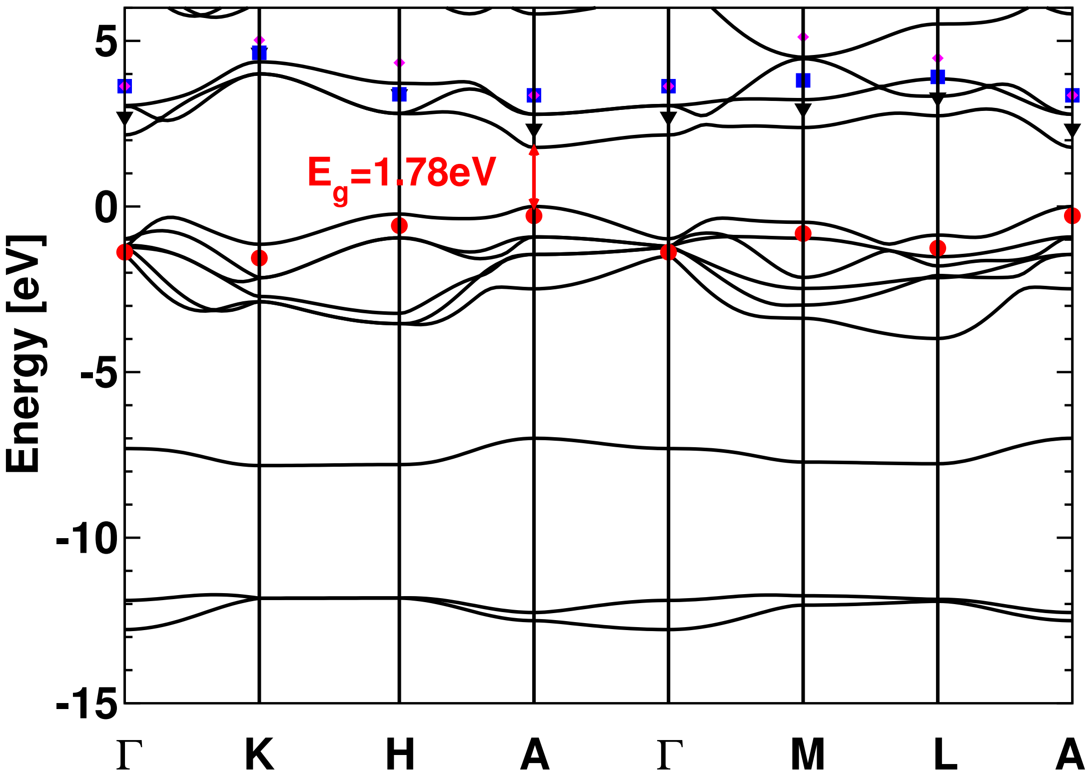

FIG. 6. DFT-LDA band structure calculation with the G0W0 corrections for the first valence band ●, and the first ▼, second ■, and third ♦ conduction bands.

extended version of Thin Solid Films 541 (2013) 9–11; https://doi.org/10.1016/j.tsf.2012.10.129

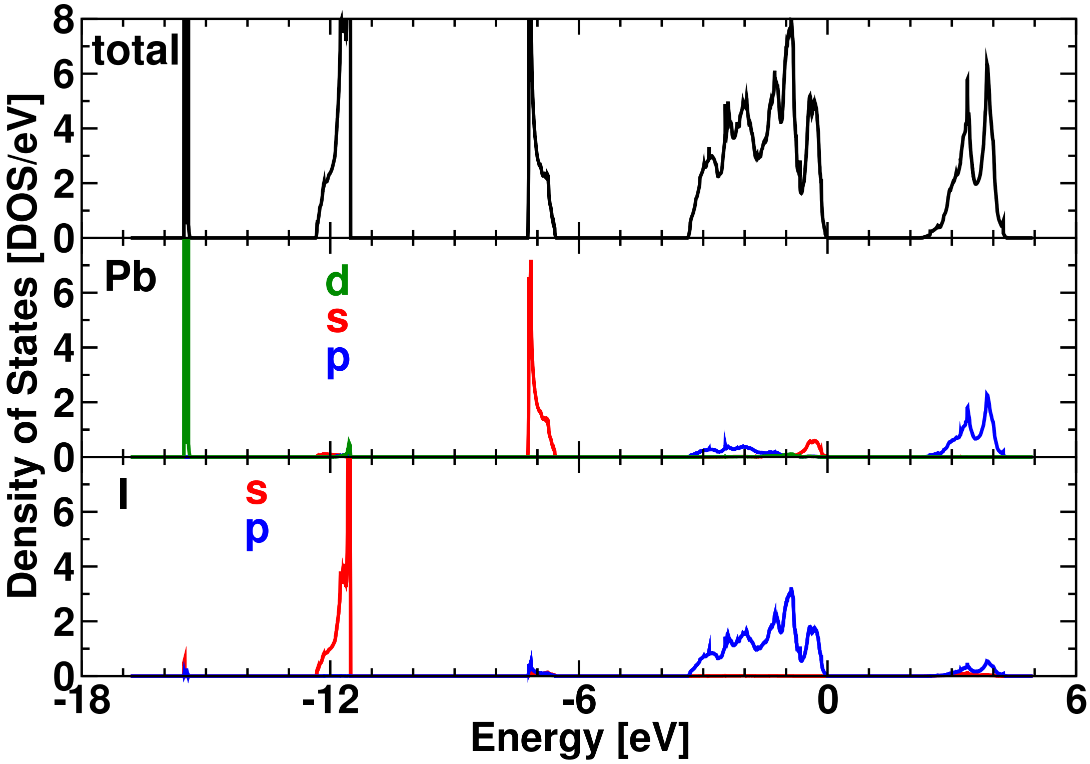

FIG. 7. Density of states and partial density of states of 2H-PbI_2

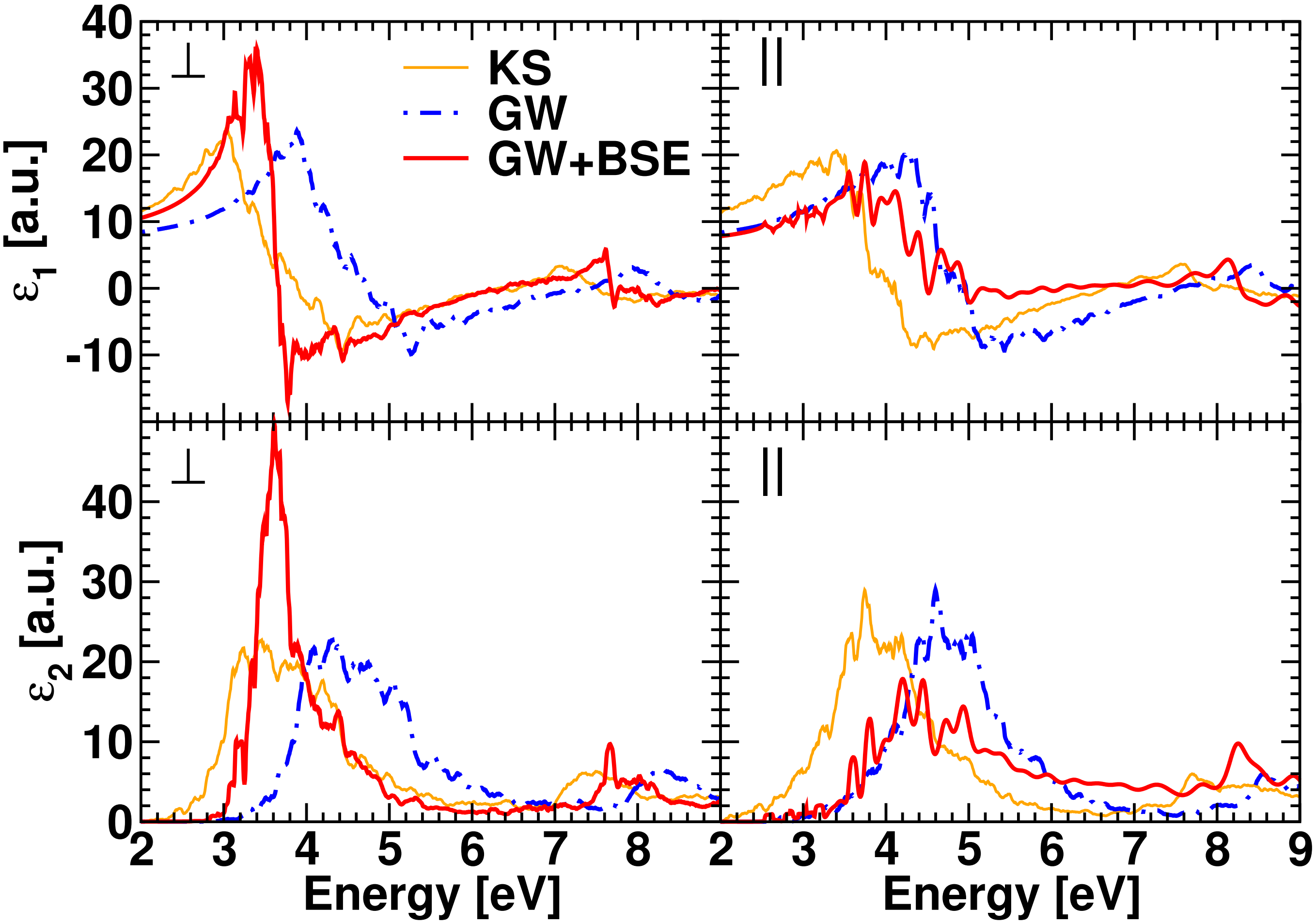

FIG. 8. Real (a) and imaginary (b) part of dielectric functions calculated by DFT, G0W0, and G0W0+BSE

extended version of Thin Solid Films 541 (2013) 9–11; https://doi.org/10.1016/j.tsf.2012.10.129

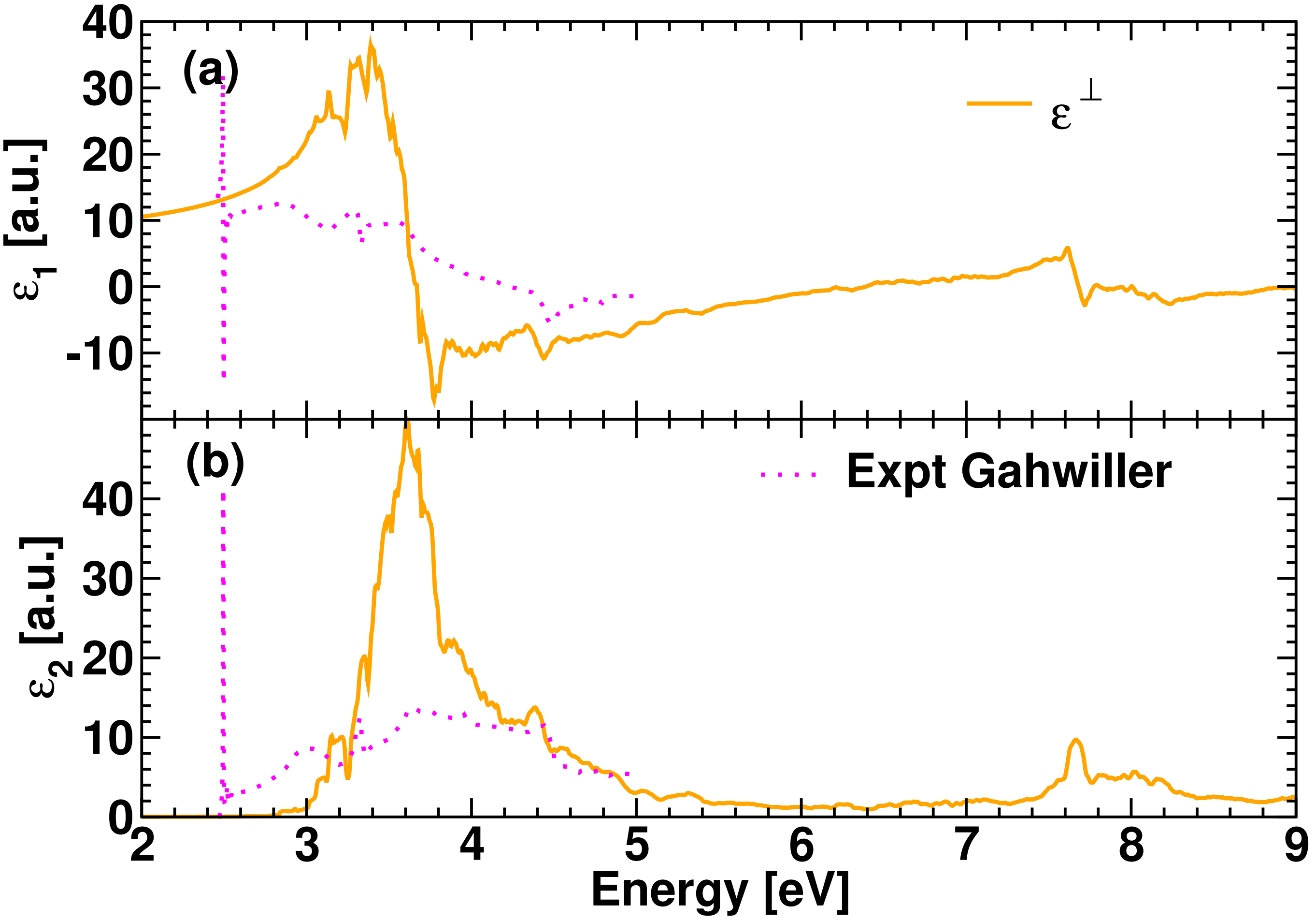

FIG. 9. Real (a) and imaginary (b) part of dielectric functions at the G0W0-BSE level compared to experiment. [11] at 77K